



Phase-dependent catalytic performance of MnO₂ for solvent-free oxidation of ethylbenzene with molecular oxygen

Jiangyong Liu^{a,*}, Haiyang Wang^a, Lixia Wang^a, Panming Jian^a, Xiaodong Yan^b

^a School of Chemistry and Chemical Engineering, Yangzhou University, Yangzhou, Jiangsu 225002, China

^b School of Chemical and Material Engineering, Jiangnan University, Wuxi, Jiangsu 214122, China

ARTICLE INFO

Keywords:

Ethylbenzene oxidation
Molecular oxygen
MnO₂
Crystal phase
O₂ activation

ABSTRACT

A green and solvent-free aerobic protocol for ethylbenzene (EB) oxidation mediated by efficient and stable solid catalysts remains a big challenge. In the present study, we report a finding of phase-dependent reactivity of MnO₂ materials with α , β , and δ phases, with the order of EB oxidation performance following δ -MnO₂ > α -MnO₂ > β -MnO₂. A clear negative correlation exists between the reactivity and average oxidation state (AOS) value of Mn, while positive correlations can be found between the reactivity and (Mn²⁺+Mn³⁺)/Mn⁴⁺ ratio and O_{II}/O_I ratio. DFT studies also validate that molecular oxygen can be adsorbed and activated much more easily over the δ -MnO₂, contributing to the generation of active oxygen species. This work provides insights into the MnO₂-based materials with different crystal phases for catalytic synthesis of high value-added chemicals.

1. Introduction

Earth-abundant and low-cost transitional metal-based oxides such as FeO_x [1–4], CoO_x [5–8] and MnO_x [9–13] have been widely used as heterogeneous catalysts in diverse catalytic applications. Among these metal oxides, MnO₂ has recently attracted great attention in oxidation reactions for environmental remediation, where crystal phase has been revealed to be an important contributor to the reaction performance [14–16]. In general, basic [MnO₆] octahedral units sharing corners and edges are arranged in different forms in different crystalline MnO₂ structures. For different catalytic reaction systems, widely varying conclusions have been formed in the comparative study of catalytic results versus crystal phases. For example, Hu and group members prepared four MnO₂ catalysts with different crystal structures for benzene combustion. It was found that the catalytic activities decreased in the order of γ -MnO₂ > β -MnO₂ > α -MnO₂ > δ -MnO₂, and the best reaction performance of γ -MnO₂ was attributed to the lowest activation energy and maximum surface adsorbed oxygen species [17]. Cheng and co-workers [18] developed three kinds of MnO₂ nanorods with different crystal phases (γ -MnO₂, β -MnO₂ and α -MnO₂). The results proved that α -MnO₂ with unique crystal phase presented the optimal activity for acetone oxidation as compared with γ -MnO₂ and β -MnO₂. Chen et al. [19] synthesized four types of MnO₂ catalysts with crystal phases corresponding to α -, β -, γ -, and δ -MnO₂ for VOC oxidation. They revealed a

quantitative correlation between the amount of specific oxygen species and the reaction rate, and different crystalline phases displayed distinct catalytic behavior, with δ -MnO₂ exhibiting the best performance for HCHO oxidation and α - and γ -MnO₂ showing superior activity in C₆H₆ oxidation. Unfortunately, despite these important explorations, most of the reported studies concentrate on the utilization of MnO₂ in the environmental catalysis field, especially for VOCs elimination. The potential application of MnO₂ in other research domains such as the catalytic synthesis of high value-added chemicals, remains largely unexplored.

As a typical ketone, acetophenone (AP) has been extensively used in perfumes and as a solvent for cellulose ethers, and it's also a very important organic intermediate for the synthesis of medicines, resins, alcohols, esters, aldehydes, etc [20–24]. EB oxidation utilizing molecular oxygen as the terminal oxidant is an important route for the manufacturing of AP, and the industrial process has been realized over the homogeneous liquid-phase oxidation system using cobalt acetate catalyst in acetic acid [23,25]. However, the need for corrosive solvents, generation of large quantities of toxic wastes and the separation limitation associated with the homogeneous catalysis are not consistent with the principles of green chemistry, and thus limit the large scale application of this process. Interest is growing in developing an efficient, environmentally friendly and low-cost heterogeneous route for AP production. A few attempts have been made, and some satisfactory

* Corresponding author.

E-mail address: liujy@yzu.edu.cn (J. Liu).

<https://doi.org/10.1016/j.apcatb.2021.121050>

Received 16 October 2021; Received in revised form 11 December 2021; Accepted 27 December 2021

Available online 29 December 2021

0926-3373/© 2021 Elsevier B.V. All rights reserved.

reaction results have been reported by using heterogeneous systems along with the adoption of solvents (initiators also required in some cases) [20,26–28]. A green and solvent-free protocol for EB oxidation catalysis mediated by efficient and stable solid catalysts remains an enormous challenge for industry and academia. Toward this end, we herein developed α -, β -, and δ -MnO₂ samples by a facile preparation strategy for the EB oxidation oriented to the production of AP. Compared with the α - and β -MnO₂, the δ -MnO₂ presents much better reaction performance. The effects of catalyst dosage, reaction time, oxygen pressure and reaction temperature on the performances were explored for the δ -MnO₂ catalyzed EB oxidation. Various characterizations and analyses were utilized for the investigation of the relationship between crystalline phases of MnO₂ and the catalytic results. The recyclability of the δ -MnO₂ was also tested, and the spent catalyst was carefully detected to check the possible changes. Kinetic analysis and DFT calculations were also performed for an in-depth understanding of the phase-dependent reaction performance. (Scheme 1).

2. Experimental

2.1. Preparation of catalysts

For the preparation of the δ -MnO₂, in a typical process, 0.3 g of KMnO₄ was first dissolved in a mixed solution of 60 mL of deionized water and 0.05 mL of ethanol. After stirring for 30 min, the mixture was transferred into an autoclave for a treatment at 180 °C for 12 h. After being naturally cooled to room temperature, the precipitate was obtained by filtration, washed repeatedly with deionized water and ethanol, and then dried at 80 °C for 12 h. The δ -MnO₂ was thus prepared. The α -MnO₂ was obtained by calcining the δ -MnO₂ at 500 °C for 2 h. For the preparation of β -MnO₂, a similar process with that of the α -MnO₂ was adopted but with the mixed solution in the solvothermal process containing 60 mL of deionized water and 1.0 mL of ethanol.

2.2. Catalyst characterizations

X-ray powder diffraction (XRD) patterns were obtained on the D8 type Advance diffractometer using Cu K α rays in the 2 θ range of 10–80 °. Raman spectra of the samples were measured on a Renishaw micro-Raman spectroscopy (Renishaw inVia Reflex). Scanning electron microscopy (SEM) images were taken on a field emission scanning electron microscope (Zeiss Supra55). Transmission electron microscopy (TEM) and high-resolution TEM (HRTEM) images were obtained using the

JEM-2100 microscope equipped with energy diffusion X-ray spectrometer (EDS). X-ray photoelectron spectroscopy (XPS) data of the samples were collected using a Thermo, Fisher Scientific ESCALAB 250Xi spectrometer. The N₂ adsorption–desorption measurements of the samples were conducted on a Quantachrome Autosorb-iQ3 sorption analyzer. The electron paramagnetic resonance (EPR) spectra were obtained on a Bruker A300–10/12 spectrometer.

2.3. Catalytic test

The prepared MnO₂ catalysts were employed for the solvent-free and additive-free oxidation of EB in the presence of molecular oxygen. The reactions were performed in a stainless steel autoclave equipped with a pressure control system. In a typical test, 0.08 g of catalyst was first dispersed in 20 mL of EB in the autoclave. Subsequently, the reactor was purged with oxygen three times. After the reactor was sealed, the autoclave was heated to 130 °C under continuous stirring, and then 0.8 MPa of oxygen was introduced and maintained during the reaction. After the reaction, the autoclave was allowed for cooling naturally, and then sampled for GC analysis on a KB-5 column with bromobenzene as an internal standard. All the oxidation products were identified by the gas chromatography–mass spectrometry (GC–MS) on an Agilent 9790 GC–MS system. For the recycling test, the spent catalyst was filtrated, washed carefully with hot deionized water and acetone, dried at 80 °C for 12 h to remove the surface impurities. The recovered catalyst was then applied in the next run. The effects of catalyst dosage, reaction time, oxygen pressure and reaction temperature on the EB oxidation catalyzed by the δ -MnO₂ were systematically performed to screen the optimal reaction conditions.

The turnover frequency (TOF) value was calculated within a low EB conversion (1 h of reaction, below 17.0%). The detailed equation is presented as follows:

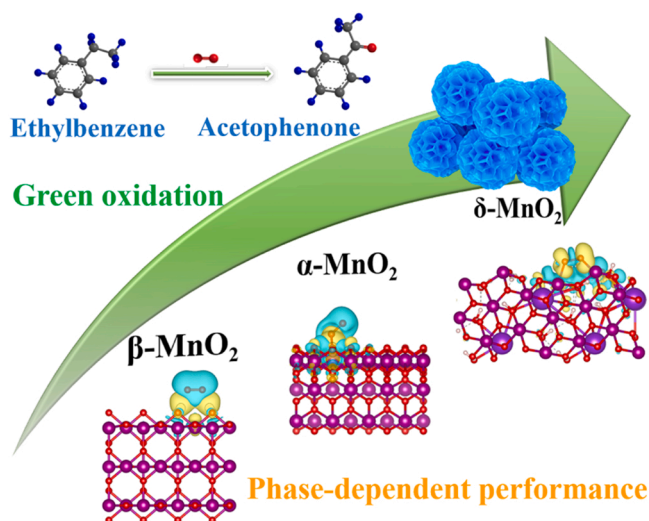
$$\text{TOF} = \frac{\text{Converted moles of EB (mol)}}{\text{Reaction time (h)} \times \text{moles of MnO}_2 \text{ (mol)}}$$

2.4. Computational models and methods

Based on the experimental observations (XRD and HRTEM results) of the three crystal phases MnO₂ (α -, β - and δ -MnO₂), the (110) facets of them were used as theoretical models to explore the performance of each MnO₂ to activate O₂. The slab models of α - and δ -MnO₂ (110) were both composed of 32 MnO₂ units (for the presence of K⁺ and H₂O, the real composition of δ -MnO₂ was KMn₄O₈·3H₂O), while β -MnO₂ (110) had 48 MnO₂ units. The atoms in the bottom half of all slab models were fixed to imitate the properties of bulk materials, while a space of 15 Å was left above to shield the effects of periodic effects in the z direction.

First-principle calculations were performed by Vienna ab initio simulation package (VASP 5.4.4) to calculate the surface properties and electronic structure of MnO₂ [29]. Perdew-Burke-Ernzerhof (PBE) form of generalized gradient approximation (GGA) was used to deal with the exchange correlation between electrons [30]. The cut-off energy of plane wave was set to 400 eV. A 2 × 2 × 1 grid Monkhorst-Pack *k*-point grid was used to sample the Brillouin area for structural relaxations and calculations of electron properties. The convergence criterion for atomic structure optimization was set to a force less than 0.01 eV/Å. All the calculations employed the PBE+*U* method with the *U* value consulted about the works of Tompsett et. al, [31,32] that (*U* - *J*) = 5.5 eV for Mn 3d electrons in MnO₂, where *J* value was set as 1.0 eV. In order to accurately describe the surface adsorption, the semi-empirical van der Waals correction method of Grimme (DFT-D3) was used to correct the dispersion interaction [33]. The crystal orbital Hamilton population (COHP) analysis for chemical bond was achieved through the lobster program [34].

The O₂ adsorption energy (*E*_{ads-O₂}) on each surface was calculated as:



Scheme 1. Schematic illustration for the EB oxidation catalyzed by MnO₂ with different crystal phases.

$$E_{ads-O_2} = E_{total} - E_{O_2} - E_{slab}$$

where E_{total} is the energy of a MnO_2 slab with one O_2 molecule adsorbing, E_{O_2} is the energy of an isolated spin triplet O_2 molecule, and E_{slab} is the energy of the MnO_2 slab.

3. Results and discussion

3.1. Morphology and phase analysis

Fig. 1a shows the XRD patterns of the samples. For the MnO_2 samples with different phase structures, the characteristic diffraction peaks can be well indexed for each phase, i.e., δ - MnO_2 (JCPDS 80-1098; P42/mnm space group; $a = b = 0.4400$ nm, $c = 0.2890$ nm), α - MnO_2 (JCPDS 44-0141; I4/m space group; $a = b = 0.9785$ nm, $c = 0.2863$ nm) and β - MnO_2 (JCPDS 24-0735; P42/mnm space group; $a = b = 0.4400$ nm, $c = 0.2874$ nm) [18,35,36]. For the three samples, δ - MnO_2 presents broader and narrower peaks than the α - MnO_2 and β - MnO_2 , which can be due to the disordered structures of δ - MnO_2 in certain crystallographic directions [14,36]. Hence, the three MnO_2 materials show remarkably different crystalline structures, i.e., rutile-structured α - MnO_2 with (2×2) tunnels, spinel-structured β - MnO_2 (1×1) , and layered-structured δ - MnO_2 $(1 \times \infty)$ [14]. Fig. 2b presents the Raman spectra of the samples. For the δ - MnO_2 , the two peaks at 570 and 630 cm^{-1} can be attributed to the M–O bonds in MnO_6 groups and M–O stretching in the basal plane of MnO_6 sheet in the layered structured δ - MnO_2 , respectively [35,37]. The α - MnO_2 is featured with four main peaks at 180, 389, 577 and 633 cm^{-1} , while the peaks at 183, 584, 645 and 750 cm^{-1} are considered to be the basic modes of β - MnO_2 [18,38,39]. The SEM and TEM images of the samples are exhibited in Fig. 2. Both the δ - MnO_2 (Fig. 2(a, a_1)) and α - MnO_2 (Fig. 2(b, b_1)) show uniform tremella-like morphologies, while the β - MnO_2 is composed of aggregated rods (Fig. 2(c, c_1)). The typical interplanar spacings of the δ - MnO_2 , α - MnO_2 and β - MnO_2 are shown in Fig. 2a₃, b₃ and c₃, respectively.

Additional structural information can be obtained from the N_2 adsorption–desorption characterizations, with the results shown in Fig. 3 and Table S1. All the three MnO_2 samples present type IV isotherms with the presence of hysteresis loops (Fig. 3a), suggesting their mesoporous structure [40,41]. The specific surface areas determined from the Brunauer–Emmett–Teller (BET) method for the δ - MnO_2 , α - MnO_2 and β - MnO_2 are 133.2, 27.0 and 25.4 $m^2 g^{-1}$, respectively. The pore volumes for the δ - MnO_2 , α - MnO_2 and β - MnO_2 are 0.59, 0.15 and 0.12 $cm^3 g^{-1}$, respectively. Fig. 3b displays the pore size distributions measured from the Barrett–Joyner–Halenda (BJH) method. The mean pore size for the δ - MnO_2 is 3.9 nm, which is slightly larger than those for the α - MnO_2 (3.1 nm) and β - MnO_2 (3.5 nm). A high surface area coupled with mesoporous structure can be beneficial for the providing of sufficient active sites and the alleviation of diffusional limitations of reactants and products within the channels [42,43].

XPS is an effective technique to acquire the information regarding surface species and electronic states of samples [44,45]. Fig. 4a presents the high-resolution XPS Mn 2p spectra of the samples, with two spin–orbit doublets at binding energies of about 641.9 and 653.3 eV indexed to $Mn2p_{3/2}$ and $Mn2p_{1/2}$, respectively. The Mn 2p spectra can be deconvoluted into five peaks, with two at around 641.1 and 652.4 eV corresponding to Mn^{3+} , the other two at 642.3 and 653.1 eV attributable to Mn^{4+} , and the one at 639.9 eV assignable to Mn^{2+} [11,46]. The ratio of $(Mn^{2+}+Mn^{3+})/Mn^{4+}$ determined by integrating the area of each peak with the fitted data is 1.78 for the δ - MnO_2 , which is higher than those for the α - MnO_2 (1.32) and β - MnO_2 (1.04). The AOS value is an important indicator of the valance state of Mn in MnO_2 [15]. The AOS value can be calculated based on the binding energy difference of Mn 3 s (ΔE_s) in Fig. 4b according to the following equation [47]:

$$AOS = 8.95 - 1.13\Delta E_s \quad (eV)$$

As listed in Table S2, the AOS values for the MnO_2 with different phases are all lower than 4, and increase in the order of δ - MnO_2 (3.31) < α - MnO_2 (3.73) < β - MnO_2 (3.94). This is in good consistence with the variation trend of $(Mn^{2+}+Mn^{3+})/Mn^{4+}$ ratio shown in Table S2, i.e., the larger the $(Mn^{2+}+Mn^{3+})/Mn^{4+}$ ratio, the smaller the AOS value. Fig. 4c presents the high-resolution XPS O 1s spectra, where the two fitted peaks at around 529.8 and 531.4 eV can be ascribed to the lattice oxygen (O_I) and surface adsorbed oxygen with low coordination (O_{II}), respectively [6,48]. As anticipated, the O_{II}/O_I ratio follows in the sequence of δ - MnO_2 (0.37) > α - MnO_2 (0.28) > β - MnO_2 (0.24), indicating the highest concentration of oxygen vacancies in the δ - MnO_2 among the three samples [49,50]. More information about the oxygen species can also be obtained from the EPR spectroscopy. As shown in Fig. S1, strong EPR signals at $g = 2.003$ related with the unpaired electrons at the oxygen vacancy sites in metal oxides [51] can be observed for the samples. The variation tendency of the signal strength shows good consistency with that of the O_{II}/O_I ratio.

3.2. Catalytic performance

The MnO_2 samples with different crystal phases were employed for the selective oxidation of EB with molecular oxygen as the oxidant in the absence of solvents and additives. As displayed in Fig. 5, among the three catalysts, the δ - MnO_2 achieves the highest EB conversion of 66.7% after 6 h of reaction. This conversion value is much higher than those for the α - MnO_2 (45.4%) and β - MnO_2 (11.7%). For all the tests, AP was detected as the main product, with 1-phenyl-ethanol (1-PA), benzaldehyde (BA) and benzoic acid (BZA) as the byproducts. The α - MnO_2 and β - MnO_2 show similar AP selectivity of 76.1% and 72.7%, respectively, while the δ - MnO_2 realizes a higher value of 89.1%. These results demonstrate that the δ - MnO_2 is a highly promising catalyst for the aerobic oxidation of EB under the challenging solvent-free and additive-free conditions.

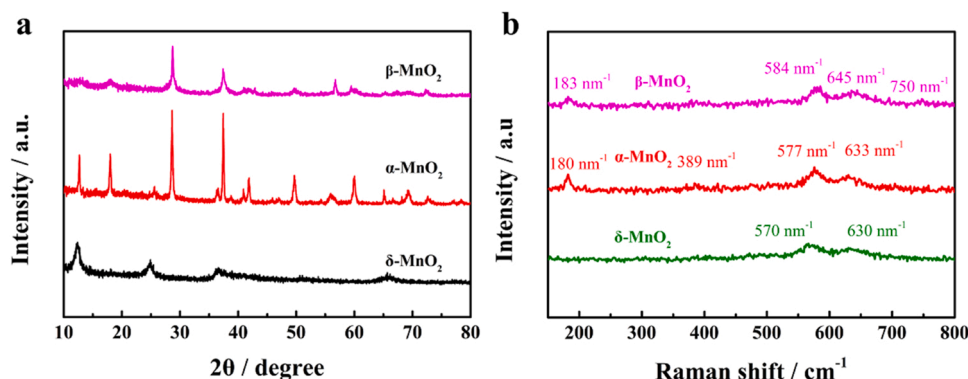


Fig. 1. XRD patterns (a) and Raman spectra (b) of the samples.

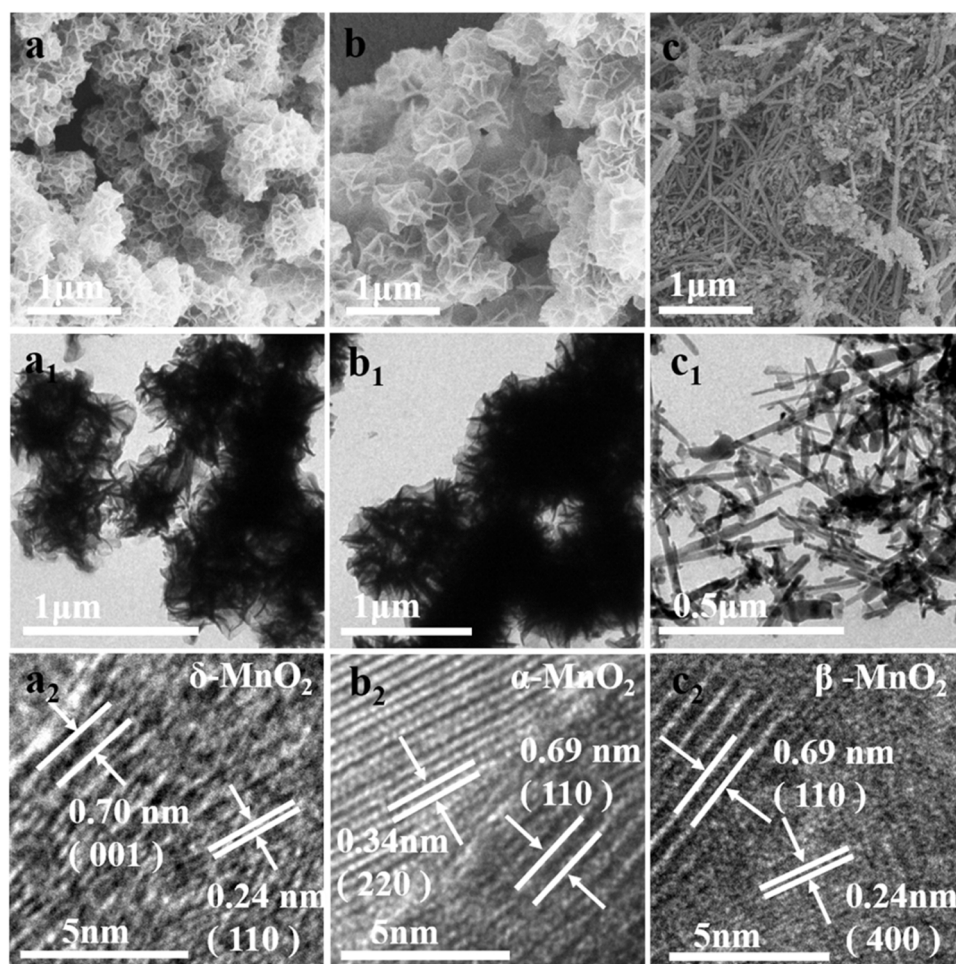


Fig. 2. SEM, TEM and HRTEM images of the MnO_2 samples with different crystal phases: $\delta\text{-MnO}_2$ (a, a_1, a_2), $\alpha\text{-MnO}_2$ (b, b_1, b_2) and $\beta\text{-MnO}_2$ (c, c_1, c_2).

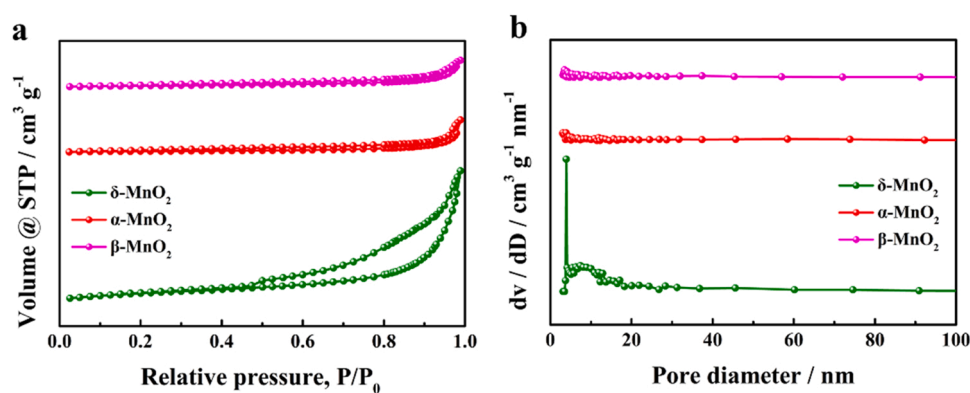


Fig. 3. N_2 adsorption-desorption isotherms (a) and pore size distributions (b) of the catalysts.

For the screening of optimal reaction conditions, a series of experiments catalyzed by the $\delta\text{-MnO}_2$ with different catalyst dosage, reaction time, oxygen pressure and reaction temperature were performed. Table S3 presents the reaction results with the $\delta\text{-MnO}_2$ dosage ranging from 0.02 to 0.10 g. The EB conversion increases from 52.6% to 72.7% with the increase of the addition of $\delta\text{-MnO}_2$ from 0.02 to 0.08 g. A further increase of $\delta\text{-MnO}_2$ dosage to 0.10 g witnesses only a small increment in conversion from 72.7% to 74.7%, while the selectivity of AP decreases slightly from 92.1% to 89.4%. This suggests that 0.08 g of $\delta\text{-MnO}_2$ is suitable for the EB oxidation, and is employed in the subsequent experiments. The reaction results for the effect of reaction time on

the EB oxidation performance are exhibited in Fig. S2. A longer reaction duration is favorable for the conversion of EB (40.7% at 3 h; 72.7% at 6 h). Only a tiny increase to 74.5% conversion of EB was obtained when the reaction was further prolonged to 7 h, accompanied with a small decrease of AP selectivity from 92.1% to 88.3% due to the overoxidation of AP. The selectivity of 1-PA gradually decreases during the reaction process, which can be attributed to the conversion of 1-PA to AP due to the activation of the $-\text{OH}$ bond in the reaction system [52]. The reaction of 6 h is an optimal duration for the $\delta\text{-MnO}_2$ mediated EB oxidation. As listed in Table S4, the EB conversion value can be remarkably enhanced from 28.9% at 0.4 MPa to 72.7% at 0.8 MPa. A higher oxygen pressure

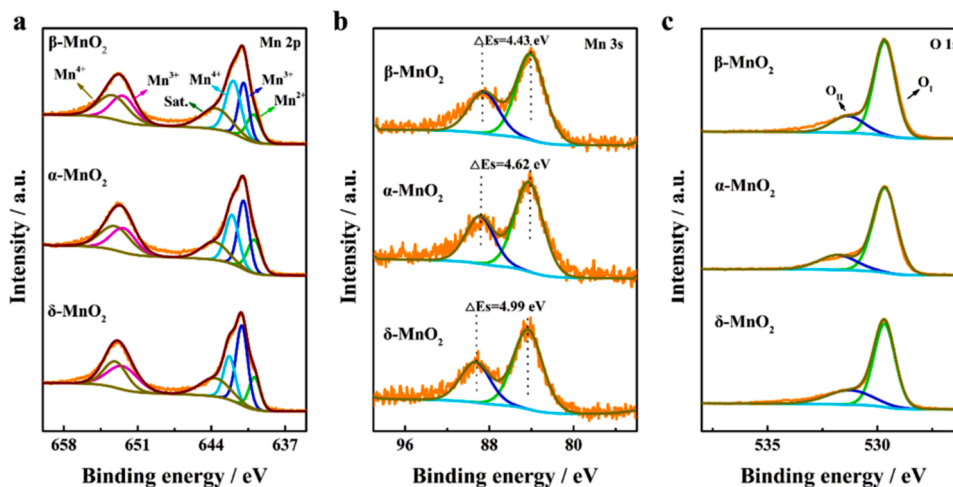


Fig. 4. High-resolution XPS Mn 2p spectra (a), Mn 3s spectra (b) and O 1s spectra (c) of the catalysts.

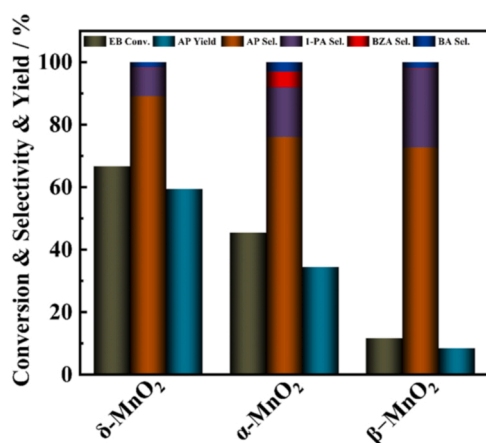


Fig. 5. MnO₂ catalysts with different crystal phases for the oxidation of EB. Reaction condition: 20 mL of EB, 0.05 g of catalyst, 130 °C, 0.8 MPa of oxygen, 6 h.

of 1.0 MPa exert negligible influence on the catalytic activity. Taking into account the economic and safety factors, an oxygen pressure of 0.8 MPa is chosen as an optimal reaction parameter in this work. Table S5 presents the influence of reaction temperature on the reaction performance, where 130 °C can be identified as the most appropriate reaction temperature for the selective oxidation of EB into AP catalyzed by the δ-MnO₂. To sum up, the optimal reaction conditions for the EB oxidation initiated by the δ-MnO₂ are using 0.08 g of δ-MnO₂ under oxygen pressure of 0.8 MPa, reaction temperature of 130 °C with reaction duration of 6 h. Under the optimal reaction conditions, the conversion of EB can achieve 72.7% with a selectivity of 92.1% to AP. Impressively, the achieved yield value of 67.0% is higher than the recent reports of 27.5% (Mn/N – C/Al₂O₃) [53], 36.9% (Cu–Ce–Co) [54], 57.6% (CeO₂/Co₃O₄-3) [55] and 63.5% (Co@GCNs-800) [56] over the same reaction system for EB oxidation (molecular oxygen as the only oxidant, and no solvents and additives used).

3.3. Probing the factors that cause performance discrepancy

Furthermore, the reaction data at different reaction temperatures were further explored for the kinetic analysis as shown in Fig. 6. It should be noted that the reaction rate values were selected at low conversions in the first 1 h of reaction, considering the influence of mass-transport limitations and catalyst deactivation. Pseudo-first-order

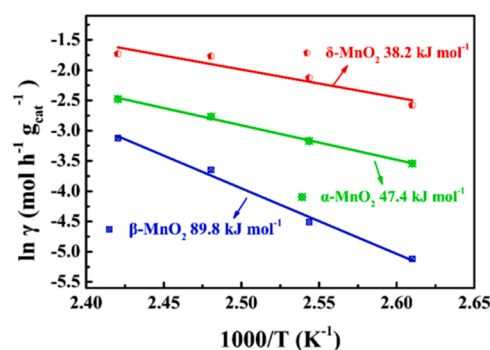


Fig. 6. Arrhenius plots for EB oxidation over MnO₂ catalysts with different crystal phases. Reaction condition: 20 mL of EB, 0.08 g of catalyst, 0.8 MPa of oxygen, 1 h.

dependence of ln γ (γ is the reaction rate defined as moles of converted EB per gram of δ-MnO₂ catalyst per hour) with respect to reaction temperature can be revealed for all the three samples. According to the Arrhenius equation, the activation energy (E_A) was determined to be 38.2 kJ mol⁻¹ for the δ-MnO₂, which is much lower than those for the α-MnO₂ (47.4 kJ mol⁻¹) and β-MnO₂ (89.8 kJ mol⁻¹). The relatively smaller E_A value indicates a lower energy barrier for the EB oxidation driven by the δ-MnO₂. Furthermore, the TOF value for the EB oxidation conducted at 130 °C with 0.08 g of catalyst was calculated within a low EB conversion (1 h of reaction, below 17.0%). Among the three MnO₂ samples, the δ-MnO₂ shows the highest TOF value of 31.0 h⁻¹, which is 2.72 and 10.7 times as that of the α-MnO₂ (11.4 h⁻¹) and β-MnO₂ (2.9 h⁻¹), respectively.

A careful correlation analysis was performed for the exploration of the factors that determine catalytic activity. Fig. S3 shows the plotting of TOF versus specific surface area, where a poor linear relationship can be observed. This suggests that reactivity is not governed by the specific surface area. Importantly, a clear negative correlation exists between the reactivity and AOS value (Fig. 7a), while positive correlations can be found between the reactivity and (Mn²⁺+Mn³⁺)/Mn⁴⁺ ratio (Fig. 7b) and O_{II}/O_I ratio (Fig. 7c). These findings demonstrate the decisive role of surface elemental compositions and chemical states in regulating the catalytic performance. In fact, as indicated from the XPS results, a larger fraction of Mn²⁺ and Mn³⁺ in MnO₂ will result in a lower AOS value and higher concentration of oxygen vacancies. Therefore, these correlations are related. A lower AOS suggests an enhanced Mn oxidation-state switching in the electron transfer process, which can trigger more oxidation/reduction redox cycles for the oxidation reactions. Previous

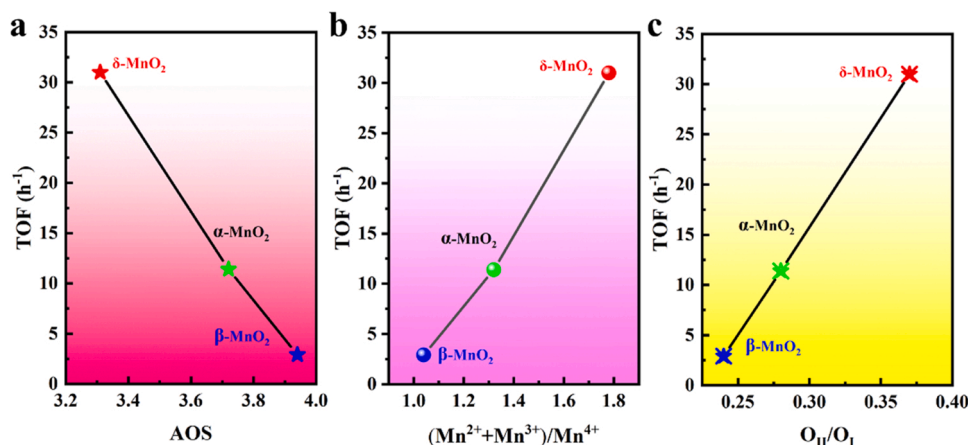


Fig. 7. TOF values for the EB oxidation catalyzed by the δ -, α - and β -MnO₂ as functions of the AOS value (a), (Mn²⁺+Mn³⁺)/Mn⁴⁺ ratio (b) and O_{II}/O_I ratio (c).

studies also found the critical effect of lower Mn oxidation states, especially Mn³⁺ on the catalytic activity of MnO₂ materials applied for the catalytic oxidation treatment of pollutants [15,46,57–59]. Mn³⁺ with d⁴ ions in the t_{2g}³e_g¹ state can result in weaker Mn–O bonds (Jahn–Teller distortion) than Mn⁴⁺ (d³), which is beneficial for the electron-transfer process due to the easy transformation of the oxidation states [14]. The charge imbalance due to the presence of Mn²⁺ and Mn³⁺ with lower oxidation states would further affect the coordination environment of oxygen species [60]. A higher oxygen vacancy amount can promote the adsorption and activation of oxygen molecules, which is favorable for the generation of more reactive oxygen species and thus accelerates oxidation process [61,62]. Hence, the MnO₂ material with lower AOS value can be speculated to be more active in the catalytic oxidation reactions. According to these findings and analyses, it is not surprising that the δ -MnO₂ displays significantly higher EB oxidation rate than the α -MnO₂ and β -MnO₂.

DFT analysis was also used to explore the phase-dependent activity of MnO₂ materials for EB oxidation catalysis. Fig. 8 presents the results of O₂ activation on α -MnO₂ (a), β -MnO₂ (b) and δ -MnO₂ (c) by comparing the amount of charge transfer and length of O–O bonds (the longer the length, the weaker the strength). Both analyses unravel the O₂ activation ability of MnO₂ with different crystal phases follow well with

the order of their catalytic performance, i.e., δ -MnO₂ > α -MnO₂ > β -MnO₂. The electronic structures of O₂ molecules adsorbed on MnO₂ surfaces were analyzed as well. According to the COHP analysis for the quantification of the strength of chemical bonds in Fig. 9(a–c), the strength of O–O bonds (corresponding to the absolute value of ICOHP) decreases in the order β -MnO₂ > α -MnO₂ > δ -MnO₂. This also shows good consistency with the results of the adsorption energies of O₂ in Fig. 9d. All these findings unambiguously demonstrate that O₂ can be adsorbed and activated much more easily over the δ -MnO₂, significantly facilitating the generation of active oxygen species. A detailed projected density of state (PDOS) analysis suggests that as the O₂ adsorption strength increases, the symmetry of spin up and down orbits increases. This can be primarily attributed to the strong orbital hybridization of the 3d electrons (Mn) with the unpaired electrons of O₂, with a main d- π _{2p} contribution from the formation of new covalent bonds.

3.4. Catalyst stability and recycling performance

Catalyst reusability is also a crucial evaluation index for the potential practical application of a heterogeneous catalyst [63,64]. This can be assessed from the recycling experiments. As illustrated in Fig. 10a, the catalytic activity and product selectivity can be well maintained in five

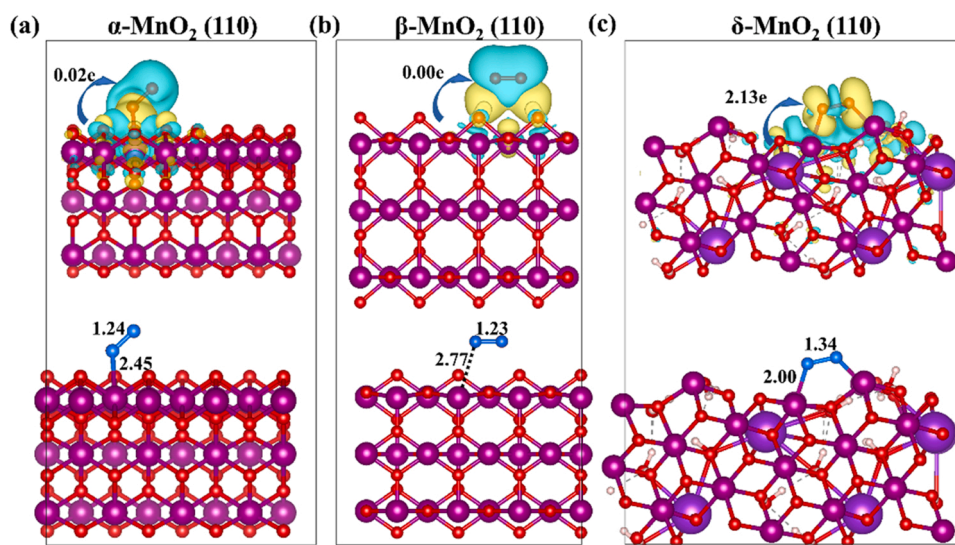


Fig. 8. Charge density differences of surface oxygen adsorptions over (a) α -MnO₂, (b) β -MnO₂ and (c) δ -MnO₂. The optimized adsorption structures are shown in the bottom of frames, in which O, Mn, H and K atoms are represented by small red, purple, white balls and large purple balls, respectively. (For interpretation of the references to colour in this figure, the reader is referred to the web version of this article.)

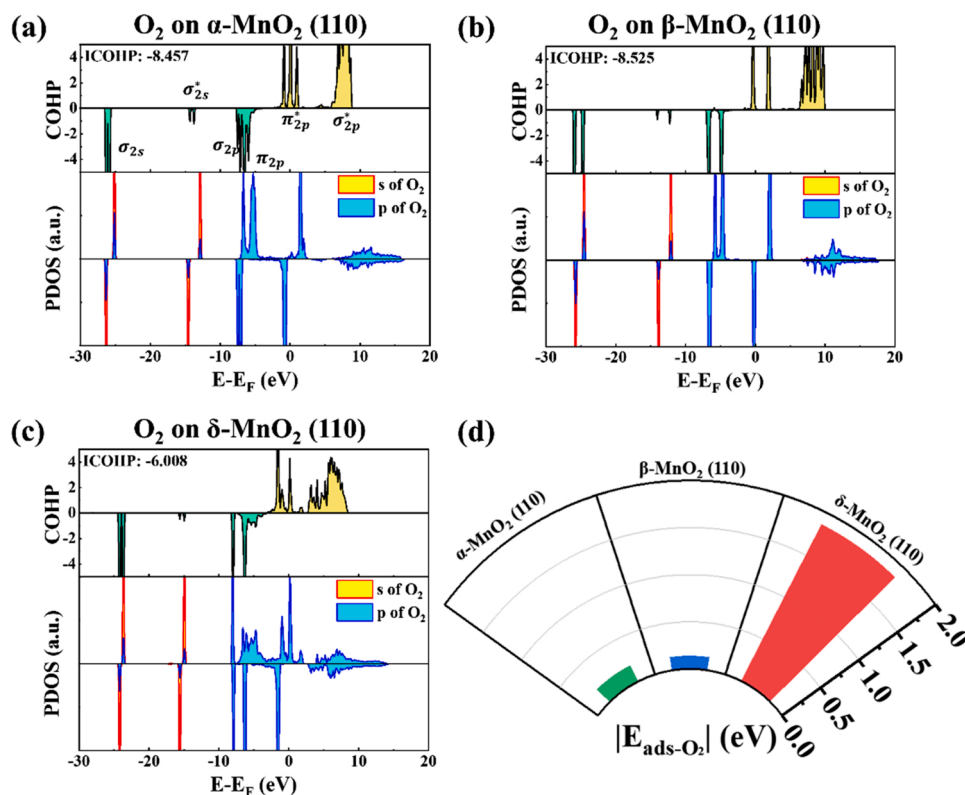


Fig. 9. COHP and PDOS of the adsorbed O_2 on (a) α - MnO_2 , (b) β - MnO_2 and (c) δ - MnO_2 and (d) the absolute values of O_2 adsorption energies on MnO_2 (110) surfaces.

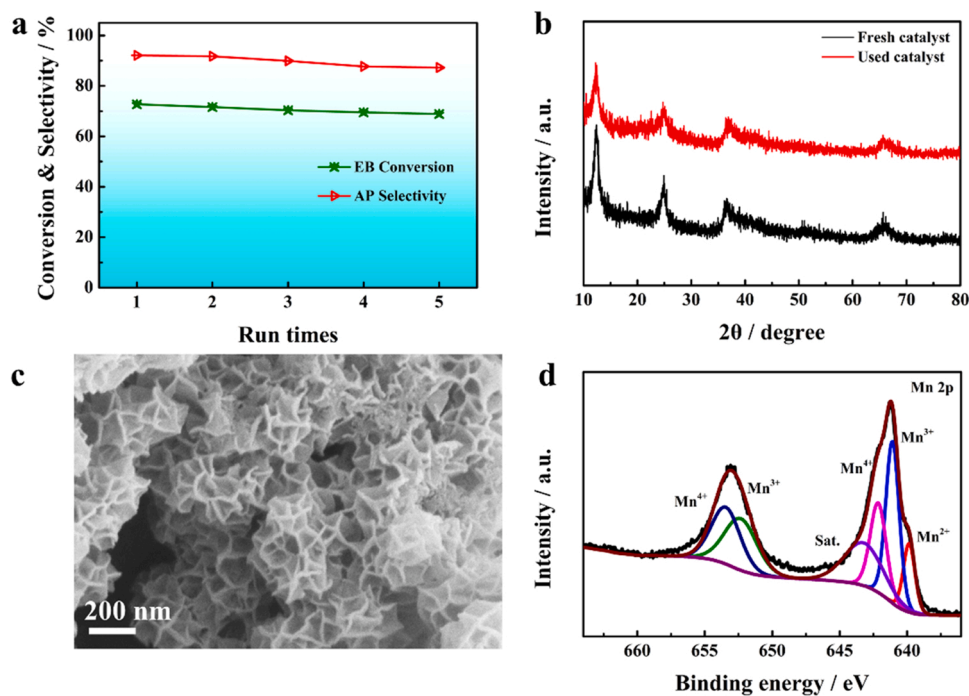


Fig. 10. (a) Recycling performance of the δ - MnO_2 catalyst in the EB oxidation reaction. Reaction condition: 20 mL of EB, 0.08 g of fresh or used δ - MnO_2 catalyst, 130 °C, 0.8 MPa of oxygen, 6 h. (b) XRD patterns of the fresh and used δ - MnO_2 catalyst. (c) SEM image and high-resolution XPS Mn 2p spectrum (d) of the used δ - MnO_2 catalyst.

consecutive runs, suggesting the good recycling performance of the δ - MnO_2 catalyst. Furthermore, the morphology (Fig. 10b) and phase structure (Fig. 10c) of the spent δ - MnO_2 catalyst is similar with those of the fresh one. These results demonstrate that the δ - MnO_2 possesses

robust stability in the EB oxidation reaction. Fig. 10d presents the high-resolution XPS Mn 2p spectrum of the spent δ - MnO_2 catalyst. The $(Mn^{2+}+Mn^{3+})/Mn^{4+}$ ratio is determined to be 1.50, which is slightly lower than that of the fresh catalyst (1.78). This suggests the partial

transformation Mn^{2+} and Mn^{3+} to Mn^{4+} during the reaction process.

4. Conclusions

In conclusion, we have facilely developed MnO_2 materials with α , β , and δ phases for the solvent-free aerobic oxidation of EB for the synthesis of AP with high added-value. The reaction results suggest that the catalytic performance for the MnO_2 catalyzed EB oxidation is highly associated with the crystal phase. Among the samples, the δ - MnO_2 presents the best performance, providing EB conversion of 72.7% and AP selectivity of 92.1%. Additionally, the δ - MnO_2 presents a much lower E_A value of 38.2 kJ mol^{-1} than the α - MnO_2 (47.4 kJ mol^{-1}) and β - MnO_2 (89.8 kJ mol^{-1}). Especially, quantitative correlations were well established between the reaction rate and the AOS value, $(\text{Mn}^{2+} + \text{Mn}^{3+})/\text{Mn}^{4+}$ ratio and O_{II}/O_I ratio. The δ - MnO_2 featured with abundant Mn oxidation/reduction redox cycles and high oxygen vacancy concentration can be favorable for the EB oxidation catalysis. With the assistance of DFT calculations, the activation of O_2 on the different phases was investigated, which reveals that the O_2 activation ability of MnO_2 with different crystal phases follows well with the order of their catalytic performance, i.e., δ - $\text{MnO}_2 > \alpha$ - $\text{MnO}_2 > \beta$ - MnO_2 . This contribution sheds light on the extended application of MnO_2 materials with various crystal structures for EB oxidation and beyond.

CRedit authorship contribution statement

Jiangyong Liu: Conceptualization, Methodology, Formal analysis, Funding acquisition, Project administration, Resources, Supervision, Validation, Writing – review & editing. **Haiyang Wang:** Data curation, Investigation, Methodology, Software, Visualization, Writing – original draft. **Lixia Wang:** Data curation, Validation, Software. **Panming Jian:** Supervision, Resources, Writing – review & editing. **Xiaodong Yan:** Data curation, Software, Writing – review & editing.

Declaration of Competing Interest

The authors declare that they have no known competing financial interests or personal relationships that could have appeared to influence the work reported in this paper.

Acknowledgements

This work was supported by the Natural Science Foundation of Jiangsu Province (BK20200956), the Jiangsu Planned Projects for Postdoctoral Research Funds (2019K093), the Natural Science Foundation of the Jiangsu Higher Education Institutions of China (17KJB530011), the Science and Technology Innovation Foundation of Yangzhou University (2019CXJ037), and the Priority Academic Program Development of Jiangsu Higher Education Institutions (PAPD). We are grateful for the support of Jie Shi from High Performance Computing Platform of BUCT.

Appendix A. Supporting information

Supplementary data associated with this article can be found in the online version at [doi:10.1016/j.apcatb.2021.121050](https://doi.org/10.1016/j.apcatb.2021.121050).

References

- [1] C. Panaritis, J. Zgheib, S.A.H. Ebrahim, M. Couillard, E.A. Baranova, Electrochemical in-situ activation of Fe-oxide nanowires for the reverse water gas shift reaction, *Appl. Catal. B* 269 (2020), 118826.
- [2] S. Huang, B.-F. Zheng, Z.-Y. Tang, X.-Q. Mai, T. Ouyang, Z.-Q. Liu, CH_3OH selective oxidation to HCHO on Z-scheme $\text{Fe}_2\text{O}_3/\text{g-C}_3\text{N}_4$ hybrid: the rate-determining step of C-H bond scission, *Chem. Eng. J.* 422 (2021), 130086.
- [3] G.W. Woyessa, J.-ab. dela Cruz, M. Rameez, C.-H. Hung, Nanocomposite catalyst of graphitic carbon nitride and Cu/Fe mixed metal oxide for electrochemical CO_2 reduction to CO, *Appl. Catal. B* 291 (2021), 120052.
- [4] M. Wang, J. Han, G. Yuan, R. Guo, Carbon/ $\text{TiO}_2/\text{Fe}_2\text{O}_3$ hybrid shells as efficient visible light photocatalysts, *N. J. Chem.* 43 (2019) 11282–11287.
- [5] T. Quast, H.B. Aiyappa, S. Saddeler, P. Wilde, Y.-T. Chen, S. Schulz, W. Schuhmann, Single-entity electrocatalysis of individual “picked-and-dropped” Co_3O_4 nanoparticles on the tip of a carbon nanoelectrode, *Angew. Chem. Int. Ed.* 60 (2021) 3576–3580.
- [6] J. Liu, R. Meng, J. Li, P. Jian, L. Wang, R. Jian, Achieving high-performance for catalytic epoxidation of styrene with uniform magnetically separable CoFe_2O_4 nanoparticles, *Appl. Catal. B* 254 (2019) 214–222.
- [7] G. Zhai, J. Wang, Z. Chen, W. An, Y. Men, Boosting soot combustion efficiency of Co_3O_4 nanocrystals via tailoring crystal facets, *Chem. Eng. J.* 337 (2018) 488–498.
- [8] J. Liu, R. Meng, H. Wang, P. Jian, Boosting styrene epoxidation via CoMn_2O_4 microspheres with unique porous yolk-shell architecture and synergistic intermetallic interaction, *J. Colloid Interface Sci.* 579 (2020) 221–232.
- [9] G. Chen, Z. Wang, F. Lin, Z. Zhang, H. Yu, B. Yan, Z. Wang, Comparative investigation on catalytic ozonation of VOCs in different types over supported MnO_x catalysts, *J. Hazard. Mater.* 391 (2020), 122218.
- [10] E. Hayashi, Y. Yamaguchi, K. Kamata, N. Tsunoda, Y. Kumagai, F. Oba, M. Hara, Effect of MnO_2 crystal structure on aerobic oxidation of 5-hydroxymethylfurfural to 2,5-furandicarboxylic acid, *J. Am. Chem. Soc.* 141 (2019) 890–900.
- [11] S. Mo, Q. Zhang, J. Li, Y. Sun, Q. Ren, S. Zou, Q. Zhang, J. Lu, M. Fu, D. Mo, J. Wu, H. Huang, D. Ye, Highly efficient mesoporous MnO_2 catalysts for the total toluene oxidation: Oxygen-Vacancy defect engineering and involved intermediates using in situ DRIFTS, *Appl. Catal. B* 264 (2020), 118464.
- [12] Y. Zhang, K. Liu, J. Wu, Z. Hu, L. Huang, J. Zhou, T. Ishihara, L. Guo, Unveiling the effects of alkali metal ions intercalated in layered MnO_2 for formaldehyde catalytic oxidation, *ACS Catal.* 10 (2020) 10021–10031.
- [13] X. Li, G. Fang, X. Qian, Q. Tian, Z-scheme heterojunction of low conduction band potential MnO_2 and biochar-based g- C_3N_4 for efficient formaldehyde degradation, *Chem. Eng. J.* 428 (2022), 131052.
- [14] J. Huang, S. Zhong, Y. Dai, C.-C. Liu, H. Zhang, Effect of MnO_2 phase structure on the oxidative reactivity toward bisphenol A degradation, *Environ. Sci. Technol.* 52 (2018) 11309–11318.
- [15] F. Nawaz, H. Cao, Y. Xie, J. Xiao, Y. Chen, Z.A. Ghazi, Selection of active phase of MnO_2 for catalytic ozonation of 4-nitrophenol, *Chemosphere* 168 (2017) 1457–1466.
- [16] F. Gao, X. Tang, H. Yi, C. Chu, N. Li, J. Li, S. Zhao, In-situ DRIFTS for the mechanistic studies of NO oxidation over α - MnO_2 , β - MnO_2 and γ - MnO_2 catalysts, *Chem. Eng. J.* 322 (2017) 525–537.
- [17] Z. Hu, R. Mi, X. Yong, S. Liu, D. Li, Y. Li, T. Zhang, Effect of crystal phase of MnO_2 with similar nanorod-shaped morphology on the catalytic performance of benzene combustion, *Chemistryselect* 4 (2019) 473–480.
- [18] L. Cheng, J. Wang, C. Zhang, B. Jin, Y. Men, Boosting acetone oxidation efficiency over MnO_2 nanorods by tailoring crystal phases, *New J. Chem.* 43 (2019) 19126–19136.
- [19] B. Chen, B. Wu, L. Yu, M. Crocker, C. Shi, Investigation into the catalytic roles of various oxygen species over different crystal phases of MnO_2 for C_6H_6 and HCHO oxidation, *ACS Catal.* 10 (2020) 6176–6187.
- [20] T. Liu, H. Cheng, L. Sun, F. Liang, C. Zhang, Z. Ying, W. Lin, F. Zhao, Synthesis of acetophenone from aerobic catalytic oxidation of ethylbenzene over Ti–Zr–Co alloy catalyst: influence of annealing conditions, *Appl. Catal. A* 512 (2016) 9–14.
- [21] W. Lv, L. Yang, B. Fan, Y. Zhao, Y. Chen, N. Lu, R. Li, Silylated MgAl LDHs intercalated with MnO_2 nanowires: highly efficient catalysts for the solvent-free aerobic oxidation of ethylbenzene, *Chem. Eng. J.* 263 (2015) 309–316.
- [22] X. Liu, S. Gao, F. Yang, S. Zhou, Y. Kong, High promoting of selective oxidation of ethylbenzene by Mn-ZSM-5 synthesized without organic template and calcination, *Res. Chem. Inter.* 46 (2020) 2817–2832.
- [23] M. Arshadi, M. Ghiaci, A.A. Ensafi, H. Karimi-Maleh, S.L. Suib, Oxidation of ethylbenzene using some recyclable cobalt nanocatalysts: the role of linker and electrochemical study, *J. Mol. Catal. A: Chem.* 338 (2011) 71–83.
- [24] X. Dai, X. Li, S. Tang, X. Peng, X. Zheng, O.J.C.C. Jiang, Efficient aerobic oxidation of ethylbenzene accelerated by Cu species in hydrotalcite, *Catal. Commun.* 149 (2021), 106184.
- [25] B. Gutmann, P. Elsner, D. Roberge, C.O.J.A.C. Kappe, Homogeneous liquid-phase oxidation of ethylbenzene to acetophenone in continuous flow mode, *ACS Catal.* 3 (2013) 2669–2676.
- [26] Y. Zhao, R. Xie, Y. Lin, G. Fan, F. Li, Highly efficient solvent-free aerobic oxidation of ethylbenzene over hybrid Zn–Cr layered double hydroxide/carbon nanotubes nanocomposite, *Catal. Commun.* 114 (2018) 65–69.
- [27] P. Zhang, H. Lu, Y. Zhou, L. Zhang, Z. Wu, S. Yang, H. Shi, Q. Zhu, Y. Chen, S. Dai, Mesoporous MnCeO_x solid solutions for low temperature and selective oxidation of hydrocarbons, *Nat. Commun.* 6 (2015) 8446.
- [28] M. Liu, S. Shi, L. Zhao, C. Chen, J. Gao, J. Xu, Aliphatic amines modified CoO nanoparticles for catalytic oxidation of aromatic hydrocarbon with molecular oxygen, *Chin. J. Catal.* 40 (2019) 1488–1493.
- [29] G. Kresse, J. Furthmüller, Efficient iterative schemes for ab initio total-energy calculations using a plane-wave basis set, *Phys. Rev. B* 54 (1996) 11169–11186.
- [30] J.P. Perdew, K. Burke, M. Ernzerhof, Generalized gradient approximation made simple, *Phys. Rev. Lett.* 77 (1996) 3865–3868.
- [31] D.A. Tompsett, D.S. Middlemiss, M.S. Islam, Importance of anisotropic coulomb interactions and exchange to the band gap and antiferromagnetism of β - MnO_2 from DFT+U, *Phys. Rev. B* 86 (2012), 205126.
- [32] D.A. Tompsett, S.C. Parker, M.S. Islam, Rutile (β -) MnO_2 surfaces and vacancy formation for high electrochemical and catalytic performance, *J. Am. Chem. Soc.* 136 (2014) 1418–1426.

- [33] S. Grimme, J. Antony, S. Ehrlich, H. Krieg, A consistent and accurate ab initio parametrization of density functional dispersion correction (Dft-D) for the 94 elements H-Pu, *J. Chem. Phys.* 132 (2010), 154104.
- [34] R. Dronskowski, P.E. Bloechl, Crystal orbital Hamilton populations (COHP): energy-resolved visualization of chemical bonding in solids based on density-functional calculations, *J. Phys. Chem.* 97 (1993) 8617–8624.
- [35] W. Xiao, W. Zhou, H. Yu, Y. Pu, Y. Zhang, C. Hu, Template synthesis of hierarchical mesoporous δ -MnO₂ hollow microspheres as electrode material for high-performance symmetric supercapacitor, *Electrochim. Acta* 264 (2018) 1–11.
- [36] J. Zhang, Y. Li, L. Wang, C. Zhang, H. He, Catalytic oxidation of formaldehyde over manganese oxides with different crystal structures, *Catal. Sci. Technol.* 5 (2015) 2305–2313.
- [37] H.-m Kim, N. Saito, D.-w Kim, Solution plasma-assisted green synthesis of MnO₂ adsorbent and removal of cationic pollutant, *J. Chem.* 2019 (2019) 1–7.
- [38] T. Barudžija, N. Cvjetićanin, D. Bajuk-Bogdanović, M. Mojić, M. Mitrić, Vibrational and electron paramagnetic resonance spectroscopic studies of β -MnO₂ and α -K MnO₂ nanorods, *J. Alloy. Compd.* 728 (2017) 259–270.
- [39] Y. Xie, Y. Yu, X. Gong, Y. Guo, Y. Guo, Y. Wang, G. Lu, Effect of the crystal plane figure on the catalytic performance of MnO₂ for the total oxidation of propane, *CrystEngComm* 17 (2015) 3005–3014.
- [40] S. Yang, J. Wang, W. Chai, J. Zhu, Y. Men, Enhanced soot oxidation activity over CuO/CeO₂ mesoporous nanosheets, *Catal. Sci. Technol.* 9 (2019) 1699–1709.
- [41] J. Liu, J. Li, R. Meng, P. Jian, L. Wang, Silver nanoparticles-decorated-Co₃O₄ porous sheets as efficient catalysts for the liquid-phase hydrogenation reduction of p-Nitrophenol, *J. Colloid Interface Sci.* 551 (2019) 261–269.
- [42] J. Liu, J. Li, R. Ye, X. Yan, L. Wang, P. Jian, Versatile bifunctional nitrogen-doped porous carbon derived from biomass in catalytic reduction of 4-nitrophenol and oxidation of styrene, *Chin. J. Catal.* 41 (2020) 1217–1229.
- [43] J. Liu, Z. Wang, Y. Sun, R. Jian, P. Jian, D. Wang, Selective synthesis of triacetin from glycerol catalyzed by HZSM-5/MCM-41 micro/mesoporous molecular sieve, *Chin. J. Chem. Eng.* 27 (2019) 1073–1078.
- [44] J. Chen, M. Wang, J. Han, R. Guo, TiO₂ nanosheet/NiO nanorod hierarchical nanostructures: p-n heterojunctions towards efficient photocatalysis, *J. Colloid Interface Sci.* 562 (2020) 313–321.
- [45] J. Liu, J. Li, P. Jian, R. Jian, Intriguing hierarchical Co@NC microflowers in situ assembled by nanoneedles: towards enhanced reduction of nitroaromatic compounds via interfacial synergistic catalysis, *J. Hazard. Mater.* 403 (2021), 123987.
- [46] X. Zheng, G. Zhang, Z. Yao, Y. Zheng, L. Shen, F. Liu, Y. Cao, S. Liang, Y. Xiao, L. Jiang, Engineering of crystal phase over porous MnO₂ with 3D morphology for highly efficient elimination of H₂S, *J. Hazard. Mater.* 411 (2021), 125180.
- [47] V.P. Santos, O.S.G.P. Soares, J.J.W. Bakker, M.F.R. Pereira, J.J.M. Órfão, J. Gascon, F. Kapteijn, J.L. Figueiredo, Structural and chemical disorder of cryptomelane promoted by alkali doping: Influence on catalytic properties, *J. Catal.* 293 (2012) 165–174.
- [48] J. Wang, L. Cheng, W. An, J. Xu, Y. Men, Boosting soot combustion efficiencies over CuO–CeO₂ catalysts with a 3DOM structure, *Catal. Sci. Technol.* 6 (2016) 7342–7350.
- [49] Y. Jian, M. Tian, C. He, J. Xiong, Z. Jiang, H. Jin, L. Zheng, R. Albilali, J.-W. Shi, Efficient propane low-temperature destruction by Co₃O₄ crystal facets engineering: unveiling the decisive role of lattice and oxygen defects and surface acid-base pairs, *Appl. Catal. B* 283 (2021), 119657.
- [50] J. Liu, H. Wang, R. Ye, P. Jian, L. Wang, Promotional effect of Mn-doping on the catalytic performance of NiO sheets for the selective oxidation of styrene, *J. Colloid Interface Sci.* 585 (2021) 61–71.
- [51] J. Wang, H. Liang, C. Zhang, B. Jin, Y. Men, Bi₂WO_{6-x} nanosheets with tunable Bi quantum dots and oxygen vacancies for photocatalytic selective oxidation of alcohols, *Appl. Catal., B* 256 (2019), 117874.
- [52] S. Pendem, R. Singuru, C. Sarkar, B. Joseph, J.-F. Lee, D.B. Shinde, Z. Lai, J. Mondal, Zeolitic imidazolate framework-mediated synthesis of Co₃O₄ nanoparticles encapsulated in n-doped graphitic carbon as an efficient catalyst for selective oxidation of hydrocarbons, *ACS Appl. Nano Mater.* 1 (2018) 4836–4851.
- [53] W.-F. Xu, W.-J. Chen, D.-C. Li, B.-H. Cheng, H. Jiang, Highly dispersed manganese based Mn/N–C/Al₂O₃ catalyst for selective oxidation of the C–H bond of ethylbenzene, *Ind. Eng. Chem. Res.* 58 (2019) 3969–3977.
- [54] S. Jie, X. Lin, Z. Chao, Z. Liu, Effective ternary copper-cerium-cobalt catalysts synthesized via a modified pechini method for selective oxidation of ethylbenzene, *Mater. Chem. Phys.* 214 (2018) 239–246.
- [55] J. Liu, R. Meng, P. Jian, R. Jian, CeO₂ nanoparticle-decorated Co₃O₄ microspheres for selective oxidation of ethylbenzene with molecular oxygen under solvent- and additive-free Conditions, *ACS Sustain. Chem. Eng.* 8 (2020) 16791–16802.
- [56] X. Lin, Z. Nie, L. Zhang, S. Mei, Y. Chen, B. Zhang, R. Zhu, Z. Liu, Nitrogen-doped carbon nanotubes encapsulate cobalt nanoparticles as efficient catalysts for aerobic and solvent-free selective oxidation of hydrocarbons, *Green. Chem.* 19 (2017) 2164–2173.
- [57] I. Zaharieva, P. Chernev, M. Risch, K. Klingan, M. Kohlhoff, A. Fischer, H. Dau, Electrosynthesis, functional, and structural characterization of a water-oxidizing manganese oxide, *Energy Environ. Sci.* 5 (2012) 7081–7089.
- [58] D.M. Robinson, Y.B. Go, M. Mui, G. Gardner, Z. Zhang, D. Mastrogiovanni, E. Garfunkel, J. Li, M. Greenblatt, G.C. Dismukes, Photochemical water oxidation by crystalline polymorphs of manganese oxides: structural requirements for catalysis, *J. Am. Chem. Soc.* 135 (2013) 3494–3501.
- [59] P.S. Nico, R.J. Zasoski, Mn(III) center availability as a rate controlling factor in the oxidation of phenol and sulfide on δ -MnO₂, *Environ. Sci. Technol.* 35 (2001) 3338–3343.
- [60] G. Zhu, J. Zhu, W. Jiang, Z. Zhang, J. Wang, Y. Zhu, Q. Zhang, Surface oxygen vacancy induced α -MnO₂ nanofiber for highly efficient ozone elimination, *Appl. Catal. B* 209 (2017) 729–737.
- [61] C. Wang, H. Yuan, G. Lu, H. Wang, Oxygen vacancies and alkaline metal boost CeO₂ catalyst for enhanced soot combustion activity: a first-principles evidence, *Appl. Catal., B* 281 (2021), 119468.
- [62] J. Liu, T. Chen, P. Jian, L. Wang, Hierarchical 0D/2D Co₃O₄ hybrids rich in oxygen vacancies as catalysts towards styrene epoxidation reaction, *Chin. J. Catal.* 39 (2018) 1942–1950.
- [63] J. Liu, T. Chen, P. Jian, L. Wang, Hierarchical hollow nickel silicate microflowers for selective oxidation of styrene, *J. Colloid Interface Sci.* 553 (2019) 606–612.
- [64] X. Chen, J. Mao, C. Liu, C. Chen, H. Cao, L. Yu, An unexpected generation of magnetically separable Se/Fe₃O₄ for catalytic degradation of polyene contaminants with molecular oxygen, *Chin. Chem. Lett.* 31 (2020) 3205–3208.